MÜHENDİSLİK FAKÜLTESİ

Uluslararası Mühendislik Araştırma ve Geliştirme Dergisi
International Journal of Engineering Research and Development

UMAGD, (2019) 11(1), 226-238.

10.29137/umagd.415901

Cilt/Volume:11 Sayı/Issue:1 Ocak/January 2019

Araştırma Makalesi / Research Article

Hydrodynamic Analysis of Shark Body Hydrofoil Using CFD Methods

Abdullah Muratoğlu

Batman University, Department of Civil Engineering, Kuyubasi Kampusu, 72100, Batman, TURKEY

***Başvuru/Received**: 17/04/2018* ***Kabul/Accepted**: 06/12/2018* ***Son Versiyon/Final Version**: 31/01/2019*

Abstract

The most efficient designs are found in the nature. Many natural events and processes have been successfully transferred to the science and technology in order to solve the problems or to increase the efficiency of the systems. The hydrodynamic principles were efficiently employed by swimming animals for many years. Excellent body shapes of fish species have enabled them to continue their generation until today. The aim of this study is to understand the 2D hydrodynamics of the tope shark (Galeorhinus galeus) and to analyze the fluid flow around its body hydrofoil. The hydrofoil of the tope shark (TSH) has been generated using a real-scale image and digitalized using NURB (Non-uniform B-spline) curves. ANSYS CFX software has been employed for CFD simulations after suitable meshing around the TSH. The pressure and velocity area around the shark hydrofoil was illustrated for different angles of attack and Re numbers. The hydrodynamic performance variables such as lift, drag and pressure coefficients for the hydrofoil were analyzed.

Key Words

''Tope Shark, CFD, ANSYS CFX, hydrofoil, biomimicry''

***Corresponding Author:** abdullah.muratoglu@batman.edu.tr*

1. INTRODUCTION

It is an indisputable fact that the most efficient and optimum designs are found in nature. Many ideas were transferred from the biology to the science and technology through bio-inspiration (Vincent et al. 2006). Imitating the geometry of humpback whales provided more efficient turbines. More sustainable buildings were constructed by mimicking the termites. Kingfishers effected high speed transportation. Mosquitos were copied for production of more efficient needles. Dolphins were imitated for better communication and signalization. Autonomous underwater vehicles (Bozkurttas et al. 2008) were designed from the fish fins. It is possible to increase the number of examples of bio-inspired technological developments (Muratoglu et al. 2016).

Two dimensional foil sections are employed in many areas such as aerial devices, wind turbines, hydrokinetic turbines and other turbomachinery. The wing sections that are utilized in technology for the last few years have already been effectively used by animals such as birds and fishes in nature for many years. Available technical problems related to fluid dynamics of aerial and submerged devices can be solved and their efficiency can be increased by mimicking from flying and swimming animals and insects (Muratoglu and Muratoglu 2017).

There are various studies investigating the hydrodynamics of fish swim together with geometrical considerations. Shrivastava et al. (2017) studied the hydrodynamics of undulating NACA 0012 hydrofoils through CFD. Xue et al. (2016) reported the hydrodynamics of bionic oscillating hydrofoil mimicking from the tuna fish and analyzed in Fluent software. The energy gain from the hydrodynamic interactions within the school of fishes has been analyzed by Hemelrijk et al. (2015). Experimental research on mechanics, kinematics, fluid dynamics and fish locomotion of various studies were reviewed by Lauder and Madden (2006). Maneuvering hydrodynamics of fish and small underwater vehicles have been studied by Bandyopadhyay (2002). The hydrodynamics of nonscombroid fish has been analyzed in order to understand the fish swimming mechanism and to calculate the thrust and power required by Webb (1978). Finally, hydrodynamics of fish-like swimming has been studied by various other scientists (Lauder and Drucker 2004; Lauder and Madden 2006; Triantafyllou 2012; Tytell 2011; Weihs 1980).

To the author's knowledge, the number of studies which measures the hydrodynamic properties of main body hydrofoil of fish species is quite limited. The body shapes of swimming animals are important contributing to their efficiency and speed based on each specie's living standards. The main objective of this study is to provide hydrodynamic analyses of 2D body hydrofoil of Tope Shark (Galeorhinus galeus) based on the hydrofoil/airfoil methodology. Galeorhinus galeus which is also called as tope shark or school shark (Camhi et al. 2009) is relatively small specie of sharks (Francis and Mulligan 1998) whose body length reaches up to 2 m. It founds at temperate waters in New Zealand, Australia, America and North Atlantic (Hurst et al. 1999) living at midwater and near the seabed.

The main body hydrofoil of the tope shark which will be called as tope shark hydrofoil (TSH) was generated. The TSH has been extracted from a real-scale image by highly used B-spline curve method. Obtained hydrofoil has been digitalized, normalized and embedded in a suitable file format. Then, the geometry has been analyzed numerically with CFD simulation techniques for different angles of attack and Reynolds numbers (Re). The pressure and velocity areas around the tope shark hydrofoil (TSH) have been outlined. Hydrodynamic performance results (lift, drag and pressure coefficients) of 2D body section were calculated.

2. THEORY and METHOD

2.1. Hydrofoil theory

The objects inside velocity fields of fluids are exposed to some physical forces. The science of hydrodynamics deals with the motion of the fluid around objects and finding out the important loads that acts on bodies. The thin cross-section unit inside a velocity field is known as foil. The foil sections are called as airfoil or hydrofoil based on the surrounding fluid such as air or water (Muratoglu 2014).

Airfoil and hydrofoils have been designed for various purposes such as aerial vehicles, turbines, propellers, fans, etc. (Yuce and Muratoglu 2015). Mainly two different resultant forces which are perpendicular to each other are generated on the section. These are lift and drag forces (Figure 1). The amount of both forces depends on the viscous stresses on the section's walls and/or the other geometrical considerations.

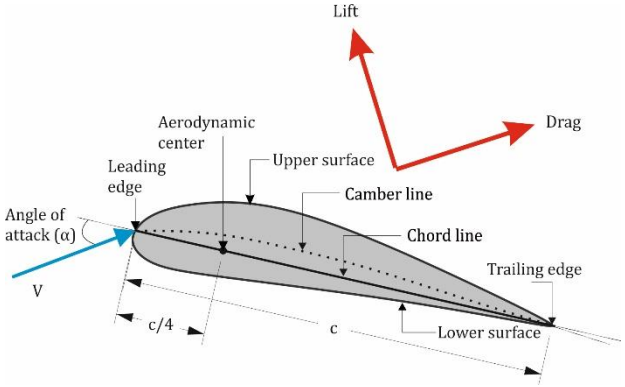

Fig. 1. Resultant loads and geometrical details of a typical hydrofoil

The lifting bodies such as hydrofoils, airfoils and vanes are designed to deliver high lift forces versus low amount of drag force (White 2010). The linear line between the leading and trailing edge is called as the chord line. If the section is not symmetrical relative to the chord line, it is called as cambered foil. The camber line is the line that passes from the vertical midpoints of the section. The angle between the free stream velocity vector and the chord line is known as the angle of attack, α (White 2010). Non-dimensionalized lift and drag forces reveals the lift and drag coefficients as below;

$$C_L = \frac{L}{\frac{1}{2}\rho V^2 A_p} \tag{1}$$

$$C_D = \frac{D}{\frac{1}{2}\rho V^2 A_p} \tag{2}$$

where, C_L is the lift coefficient, C_D is the drag coefficient, L and D are the total lift and drag forces developed on the profile, ρ is the density of the surrounding fluid, V is the velocity of the flow, A_p is the projected area.

The pressure coefficient (C_p) is a non-dimensional parameter which is extensively used in aero-hydrodynamics, even more than the pressure itself. It is a measure showing the amount of deviation of local pressure from the free stream static pressure (Anderson Jr 2011). Increasing the absolute value of pressure coefficient results higher risk of cavitation and thus damages the section (Rubenstein et al. 2012). The pressure coefficient can be defined as follows;

$$C_p = \frac{P - P_\infty}{\frac{1}{2}\rho V^2} \tag{3}$$

where, C_p is the pressure coefficient, P is the local static pressure, P_∞ is the free stream static pressure.

2.2. Extraction of 2D hydrofoil

Various studies were reported (Dahl and Fuglsang 1998; Grasso 2012; Mauclère 2009) that the airfoil or hydrofoil surfaces can be well described using non-uniform rational B-spline curves (NURBS). These curves are generated using a number of nodes and a single curve is produced based on the Cartesian coordinates of the nodes and the degree of the spline. Majority of 2D and 3D modeling software are capable of drawing NURBS. The complex details on object parts could be easily stated by B-spline curves (Wang et al. 2013). Increased number of nodes or control points (CP) provides more flexible geometries however more lively curves can be generated using smaller number of CP's (Dahl and Fuglsang 1998).

In this study, a real-scale image of a Tope Shark (Galeorhinus galeus) has been used. The leading and trailing edges were determined and the hydrofoil body is normalized to obtain a chord length of 1 m. The caudal, pectoral, anal dorsal and pelvic fins were excluded from the main body (Figure 2) of the 2D shark image. Then, a 3rd degree B-spline curve is fitted to the remaining part with 15 CP's via MATLAB software. B-spline operation was carefully conducted around the leading edge site for a more precise expression of the geometry. The number of CP's was increased around the curved zones such as leading edge and lower surface of the body (Figure 3). A sharp (blunt) trailing edge (TE) was preferred for effective meshing and simulation. For this purpose, the trailing edge triangle was cut at 2c/1000 length from the right hand side (Figure 4). After normalization, the final XY coordinates of the B-Spline curve have been excluded as a suitable file format for the geometry processing software before meshing and hydrodynamic simulations.

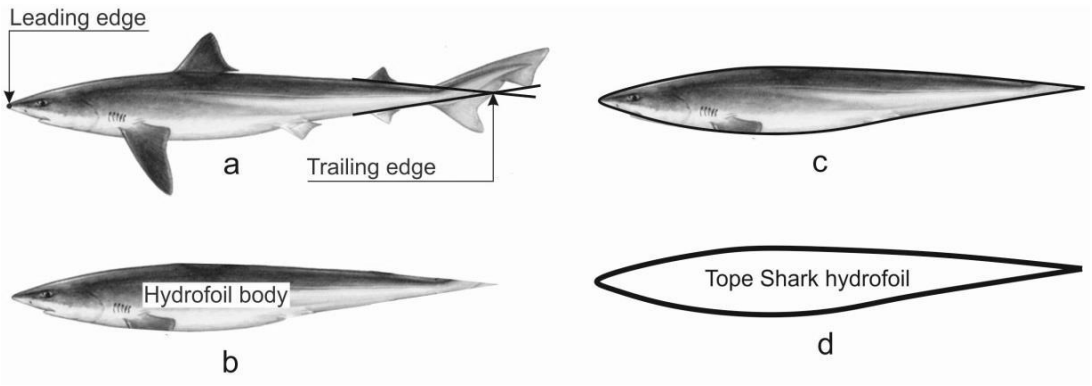

Fig. 2. Hydrofoil production from Tope Shark body geometry

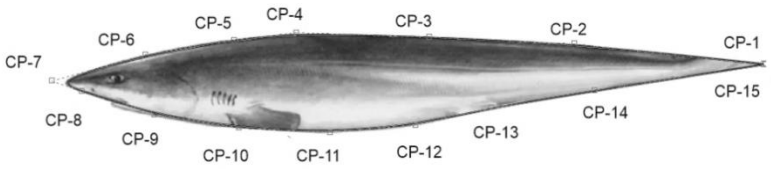

Fig. 3. Control points and resulting B-spline curve

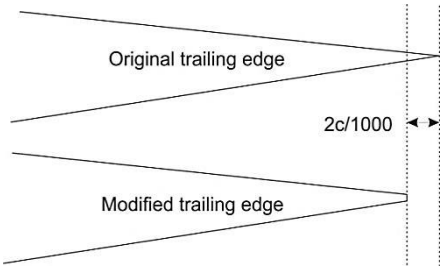

Fig. 4. Trailing edge modification

2.3. Numerical Setup

The extracted hydrofoil of Galeorhinus galeus were introduced to the ANSYS SpaceClaim software for generating the solution domain. The horizontal distance between leading edge (LE) and inlet has been specified to be 5 times of the chord length. The solution domain has been defined to be C type for being compatible with the LE. The distances at the hydrofoil wake and farfield were assigned to be 10 times of the chord (Figure 5).

The inlet boundary condition (BC) was chosen to be velocity type. The free stream velocity, thus the Re number around the hydrofoil can be defined at the inlet. The outlet was specified to be pressure type with a subsonic flow regime at 1.5 atm. Medium turbulence intensity with 5 % has been assigned for turbidity. The hydrofoil walls were specified with no-slip condition in order of ability of capturing the viscous effects near the profile. Both planar sides of the 2D domain were qualified as symmetry planes (Figure 5).

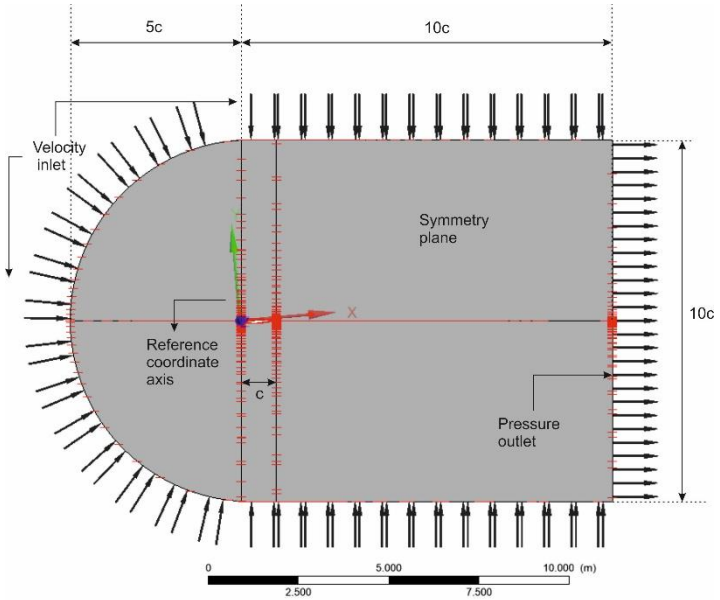

Fig. 5. Illustration of solution domain

The grid generation inside the fluid domain is provided using structured quadrilateral type of cells. Approximately 600,000 nodes and and 300,000 elements were generated inside the domain. Produced mesh has been refined toward to the leading edge, trailing edge and hydrofoil walls. Mapped face meshing with edge sizing operation employing a suitable bias factor was employed for grid densification. The detailed images of improved mesh for the whole domain, around the hydrofoil, leading and trailing edges were illustrated in Figure 6, respectively.

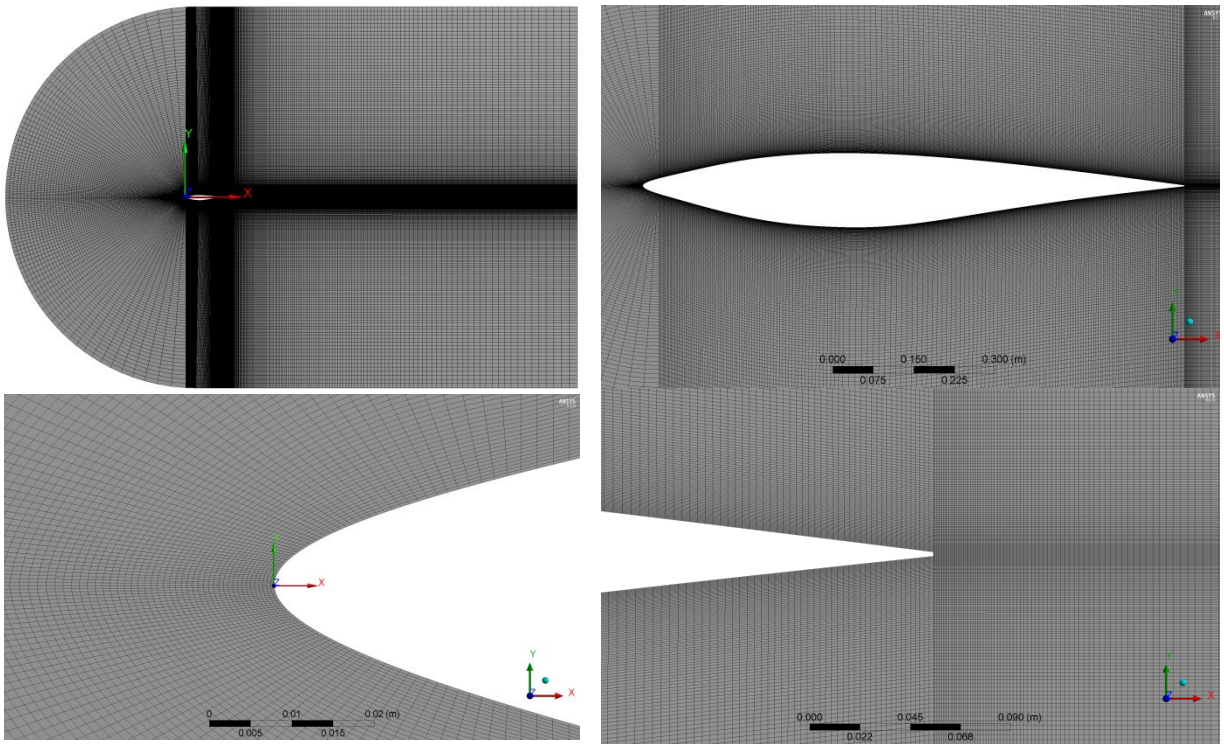

Fig. 6. Structured grid generation around computational domain

2.4. Turbulence model

In the present study, SST (Shear Stress Transport) turbulence model has been employed with automatic wall function. The model is one of the most widely used two-equation eddy viscosity approaches. Integrating k-ω and k-ε models, SST used advantages of both models. In SST model, the viscous near wall layers are modeled with the advantages of Wilcox's k-ω approach and the far-field region away from the viscous effects is modeled by the k-ε approach. Combining the advantages of both widely used turbulence models makes SST method to be one of the most successful models (Muratoglu and Muratoglu 2017). k and ω equations are given by (Versteeg and Malalasekera 2007) as below;

The *k* equation is;

$$\underbrace{\frac{\partial(\rho k)}{\partial t}}_{\substack{\text{rate of}\\ \text{change}\\ \text{of } k}} + \underbrace{div(\rho k\mathbf{U})}_{\substack{\text{transport of } k\\ \text{by convection}}} = \underbrace{div\left[\left(\mu+\frac{\mu_t}{\sigma_k}\right)grad(k)\right]}_{\substack{\text{transport of } k \text{ by turbulent diffusion}}} + \underbrace{\left(2\mu S_{ij}.S_{ij}-\frac{2}{3}\rho k\frac{\partial U_i}{\partial x_j}\delta_{ij}\right)}_{\substack{\text{production}\\ \text{rate of } k}} - \underbrace{\beta_1\rho k\omega}_{\substack{\text{dissipation}\\ \text{rate of } k}} \quad (4)$$

The omega equation is;

$$\underbrace{\frac{\partial(\rho\omega)}{\partial t}}_{\substack{\text{rate of}\\ \text{change}\\ \text{of } \omega}} + \underbrace{div(\rho\omega\mathbf{U})}_{\substack{\text{transport of } \omega\\ \text{by convection}}} = \underbrace{div\left[\left(\mu+\frac{\mu_t}{\sigma_{\omega,1}}\right)grad(\omega)\right]}_{\substack{\text{transport of } \omega \text{ by turbulent diffusion}}} + \underbrace{\gamma_2\left(2\rho S_{ij}.S_{ij}-\frac{2}{3}\rho\omega\frac{\partial U_i}{\partial x_j}\delta_{ij}\right)}_{\substack{\text{production}\\ \text{rate of } \omega}} - \underbrace{\beta_2\rho\omega^2}_{\substack{\text{dissipation}\\ \text{rate of } \omega}} + \underbrace{2\frac{\rho}{\sigma_{\omega,2}\omega}\frac{\partial k}{\partial x_k}\frac{\partial \omega}{\partial x_k}}_{\substack{\text{cross diffusion term}}} \quad (5)$$

where; k is the turbulent kinetic energy (m^2/s^2), ε (epsilon) is the turbulence eddy dissipation rate (m^2/s^3), ω (omega) is the turbulence frequency ($\omega = \varepsilon/k$), **U** is the average velocity vector, μ is the fluid's viscosity, μ_t is the turbulent or eddy viscosity ($\mu_t = \rho k/\omega$), δ_{ij} is the Kronecker delta, *div* is the mathematical divergence operator, *grad* is the mathematical gradient operator, S is the deformation rate of fluid for mean flow and the cross diffusion term arises from $\varepsilon = k\omega$ transport in the epsilon equation. The model constants are; σ_k=1, $\sigma_{\omega,1}$=2, $\sigma_{\omega,2}$=1.17, γ_2=0.44, β_1=0.09 and β_2=0.083.

2.5. y^+ value

The y^+ value describes the size of mesh which is adjacent to the walls for no-slip condition. The height or location of the first cell is directly effects the behavior of the flow. The turbulent flow can be divided into 4 layers which are viscous sublayer, buffer layer, overlap layer and turbulent layer (from the wall toward to the far field). The height of the viscous sublayer is dimensionally insignificant. However, this tiny layer has a very important function determining the characteristics of the whole flow due to the high velocity gradients. The thickness of this layer is directly proportional to the kinematic viscosity and inversely proportional with the average stream velocity (Çengel and Cimbala 2006). The mathematical description of y^+ can be defined as below;

$$y = \frac{5\nu}{u_*} \tag{6}$$

$$y^+ = \frac{u}{u_*} = \frac{yu_*}{\nu} \tag{7}$$

$$u_* = \sqrt{\frac{\sigma_w}{\rho}} \tag{8}$$

where, y is the vertical distance from the wall, ν is the kinematic viscosity, u is the flow velocity, u_* is friction velocity, y^+ is the non-dimensionalized distance from the wall.

For an accurate CFD analysis, the first cell next to the wall should be inside the viscous sublayer. It is a common operation to minimize the y^+ value in CFD simulations. If the logarithmic wall function is specified, the centroid of the first grid should be placed between 30 and 300 non-dimensional distance. For resolved wall treatment the amount of y^+ value is suggested to be below 1 (ANSYS 2011). However, for good drag prediction and efficiently modeling of the turbulence, a y^+ value of 5 or less is sufficient. In this study, automatic wall function has been employed and Figure 7 illustrates the y^+ value around the hydrofoil wall. According to the figure, amount of y^+ varies at the different regions on the wall between 1 and 4. The leading edge site is the most sensitive region of the section. Employing automatic wall function and proximity to 1 makes the y+ value to be acceptable in this study.

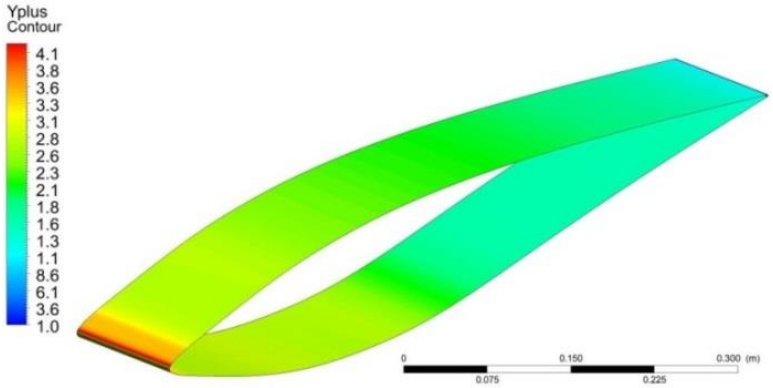

Fig. 7. y+ value around the hydrofoil wall

3. RESULTS AND DISCUSSION

3.1. CFD solution and convergence

A typical convergence diagram for the CFD analyses is given in Figure 8. In all simulations, the solution was converged with root mean square (RMS) of variables below $1x10^{-6}$. The imbalances in the domain have generally been noted to be zero or very small such as ±1/10000. The convergence criteria have been reached approximately at 100 iterations using a computer having i7-6700HQ processor with 24 GB ram and 4 GB graphics card.

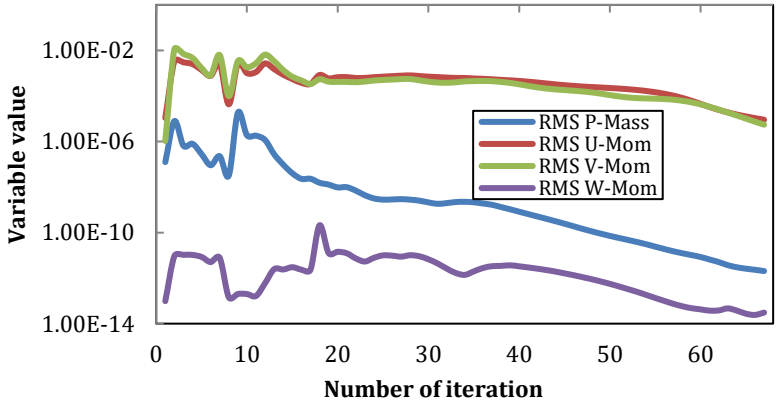

Fig. 8. A typical convergence diagram

CFD analyses have been provided for the various cases which are listed in Table 1. Totally results of eight CFD analyses have been reported in this study. The convergence of the post stall region especially after α=10° hardly exceeded the termination criteria of the software which is either the maximum number of iterations or RMS values of residuals. Considering the necessity of the residuals to be lower than $1x10^{-6}$, the solutions that is not converged (for lower Re numbers and higher values of α) below this amount has not been reported in this study.

Table 1. CFD analyses reported in this study for various cases

Re/α	0°	3°	5°	7°
1.00E+05	+	+	+	+
1.00E+06	+	+	+	+

3.2. Accuracy and acceptability of the results

The CFD analysis results with available mesh and other solution specifications has been verified comparing the airfoil performance characteristics with the JavaFoil (Hepperle 2014) software. The lift performance of the TSH (tope shark hydrofoil) has been calculated using both ANSYS CFX and JavaFoil software.

Figure 9 illustrates the comparison of lift coefficients obtained from both JavaFoil and CFX software. CFD analyses are time consuming operations relative to the 2D panel codes such as JavaFoil or Xfoil. Therefore four CFD simulations (at α=0°, 5°, 7° and 10°) has been operated and compared with wide range of JavaFoil (bold/black line) results (-15° ≤ α ≤15°). The simulation outputs represent good consistency with the numerical results of the panel code for both pre and post-stall regions having around 10 % average error which is appropriate for most of the cases. The verification stage shows the acceptability of the simulation results and accuracy of the CFD analyses.

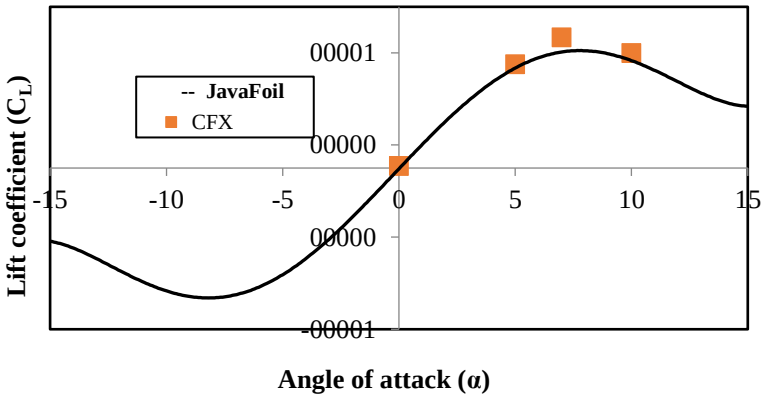

Fig. 9. Validation of the model (Comparison of JavaFoil and CFX results)

3.3. Visualization of the flow fields

The simulation results are important in order to understand the flow field around the TSH at different cases. Figures 10 and 11 illustrates the pressure and velocity fields around the TSH for Re=1 million. Lift and drag forces develop from the net pressure difference on both sides of the fish body foil. The geometrical considerations necessitates the flow velocity to be higher at the upper surface than the lower surface (Bone and Moore 2013). The pressure contour plot (Figure 10) shows that high pressure zone is developed at the leading edge site immediately below the surface. Also the total pressure of upper surface decreases with increasing angle of attack (the green region). These pressure disturbances show that a clockwise pitching moment would develop with a relatively lower lift. Also, the leading edge site seems to be the most sensitive region for cavitation risk.

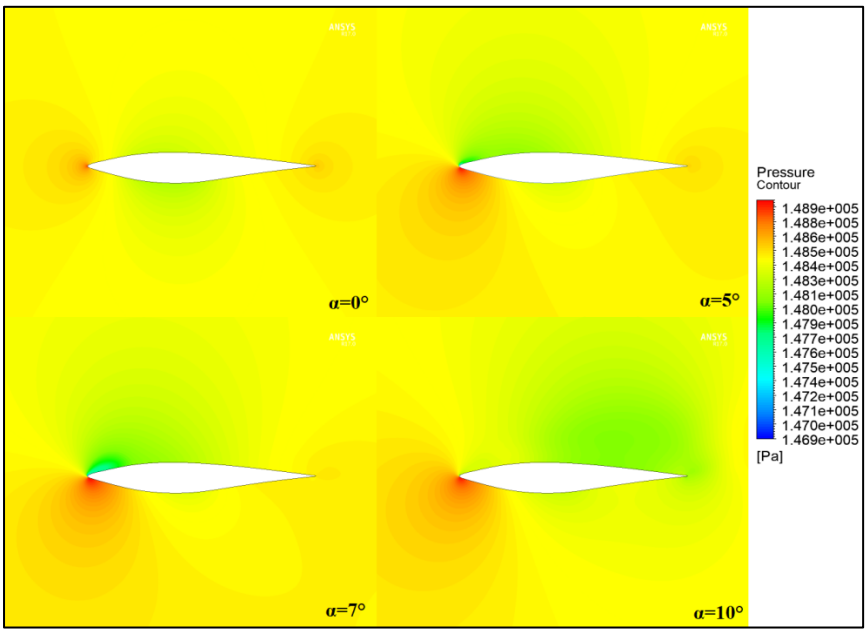

Fig. 10 . Pressure contours at various α for Re=1 million

The velocity contour plot (Figure 11) shows that for α=0˚ the water speeds around both upper and lower surfaces are close to each other and the lift force at the smaller angles of attack is relatively low due to nearly symmetrical geometry. The velocity at the boundary layer of the wall is observed to be approximating to zero (blue region) at each case due to the viscous effects around the wall. Increasing α expands the high speed zone (red color) above the boundary layer of upper surface, also extends the flow separation zone which is shown as blue. It is observed that, the TSH is at the condition of stall at α=10˚ due to the flow separation.

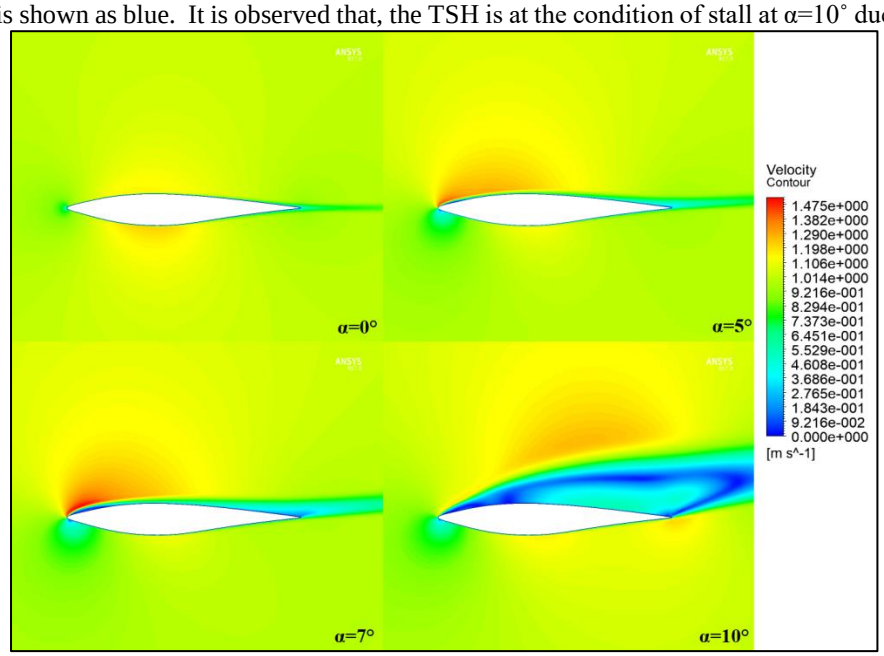

Fig. 11 . Velocity contours at various α for Re=1 million

3.4. Lift, drag and pressure coefficients

Lift and drag coefficients and L/D (lift/drag) ratios obtained from each simulation are shown in Figures 12 and 13 for Reynolds numbers of 0.1 million and 1 million, respectively. The blue squares represent the lift coefficient (C_L) or drag coefficient (C_D) of each simulation having different angles of attack. 2nd degree polynomial curves are fitted to the CFD results to see the lift and drag behavior of the TSH. The simulations at both Re numbers reveals a stall angle around 7-8 degrees which is also verified by JavaFoil results (Figure 9). Beyond the 8˚ stall angle, the lift performance is deteriorating and the drag coefficient increases exponentially. Cross comparison of both figures demonstrates those both C_L and C_D remain more or less unchanged with increasing Re number. This result shows that the variations in TSH swimming speed do not affect the performance behavior of Tope Shark; demonstrating the body shape of the tope shark is appropriate for a wide range of swimming velocities and is suitable for both cruising velocities and burst of speed.

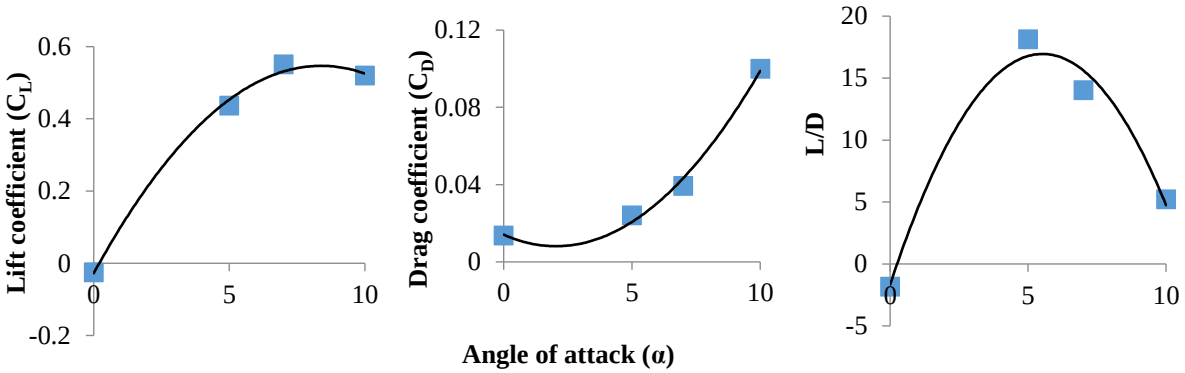

Fig. 12. Lift and drag coefficient distributions of TSH at various α for Re=0.1 million

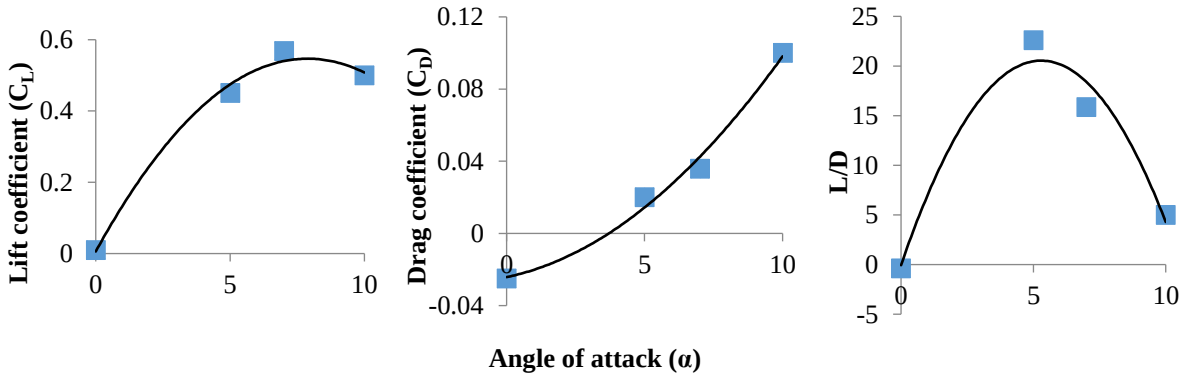

Fig. 13. Lift and drag coefficient distributions of TSH at various α for Re=1 million

The L/D ratio is one of the most important parameters showing the performance of man-designed blade sections. The industrial sections which are developed for aerial or turbomachinery purposes deliver higher lift together with some other special design criteria. However, providing high lift could not be the main specification of natural designs. Similarly, a high lift body shape may harm the fish by blocking its transportation and other living comfort by which the TSH's relatively lower L/D could be better explained.

The pressure coefficient (C_P) which shows the local pressure relative to the free stream static pressure around TSH is shown in Figure 14. Figure 10 can also be taken into account for better understanding of high and low pressure regions around the section. Both figures indicates that, the C_p of TSH at Re=1 million is relatively lower than the industrial blade sections. These results represents, the TSH has lower risk of cavitation which is an expected situation for a section that is naturally designed for large Re intervals. On the other hand, the maximum deviation of the C_p is observed to be close to the stall condition at α=7°. At post-stall region (α=10°) the pressure deviations becomes smaller.

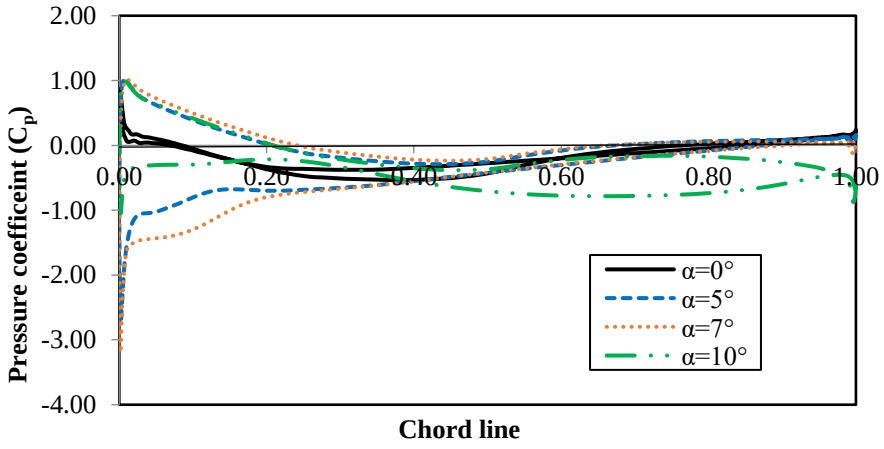

Fig. 14. Pressure coefficients around the chord line at Re=1 million

3.5. Comparison with the other airfoils

In this section, the outcomes of this study have been compared to the airfoils generated from some other swimming animals and with widely used aeronautical sections (NACA, NREL, RISØ). While there is quite high number of studies in the literature analyzing 2D or 3D performances of man-designed airfoils, hydrofoils or blade sections, the studies examining the naturally optimized sections are quite limited. Detailed hydrodynamic analyses of grass carp, sockeye salmon and blue marlin fish species have been provided by (Muratoglu et al. 2016) based on the airfoil methodology (Figure 15). Mentioned study considers several fish body shapes in order to adapt their excluded geometries to the aviation and marine industries. They conclude that, 2D carp airfoil has a stall angle around 13 degrees at a wide Re interval. Again, the lift coefficient is evaluated to be greater than 1.0 at Re=10,000. On the other hand, marlin fish airfoil has relatively lower lift coefficient owing to it extraordinary body shape. Stall angle of the marlin fish was found to be very low which is an expected situation for thin and elongated foils due to encountering lower pressure drag. Similarly, salmon and carp fish geometries are found to be of high lift coefficient while shark body shape delivered relatively lower performance.

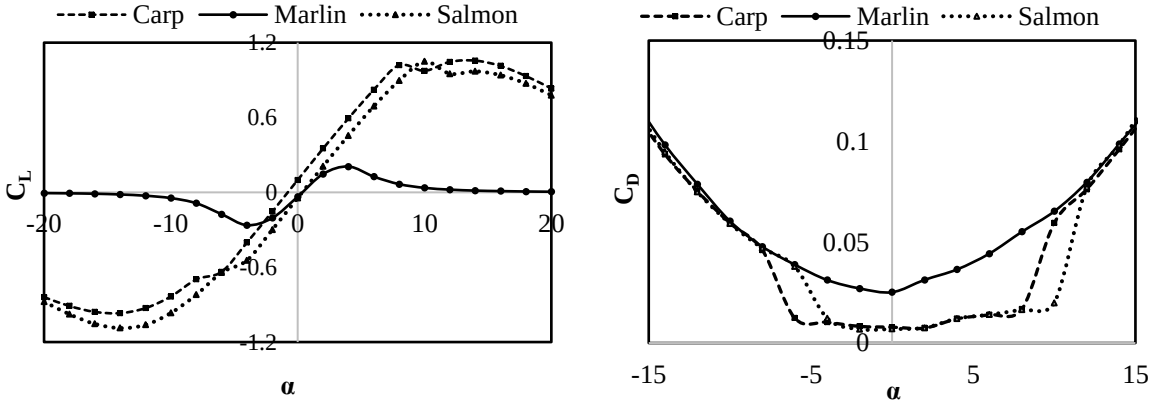

Fig. 15. Lift and drag coefficients of Carp, Marlin and Salmon fishes vs. angle of attack (Muratoglu et al. 2016)

Detailed analyses on hydrodynamic characteristics of tuna fish hydrofoil (Albacore tuna) has been provided by (Muratoglu and Muratoglu 2017). Albacore tuna has a well streamlined, nearly symmetrical body shape cruising around 6-8 m/s speed with relatively higher rate of Re number. A smooth stall behavior had been observed in which sudden fluctuations in lift and drag coefficients are not available. Also, maximum lift coefficient of tuna fish hydrofoil has been evaluated to be slightly lower than 1.0 at a stall angle around 13°. The drag characteristic of the mentioned section is found to be reasonable compared to the NACA sections. However, the pressure coefficients at different angles of attack were found to be relatively higher especially at the upper surface (exceeding -7 at α=15° and Re=1 million) which would limit its applicability in marine vehicles. In the present study, TSH represented lower pressure coefficient at the suction side relative to the tuna fish hydrofoil. Velocity distributions of Albacore tuna fish hydrofoil has been illustrated in Figure 16. The flow separation of tuna fish geometry develops at the trailing edge site, while the TSH analyzed in this study delivers a separation point close to the leading edge (Figure 11). Flow separation behavior of both geometries directly affects the stall characteristics and maximum lift coefficients in which the hydrodynamic performance of the TSH is said to be lower than tuna fish hydrofoil based on net lift force developed on the section.

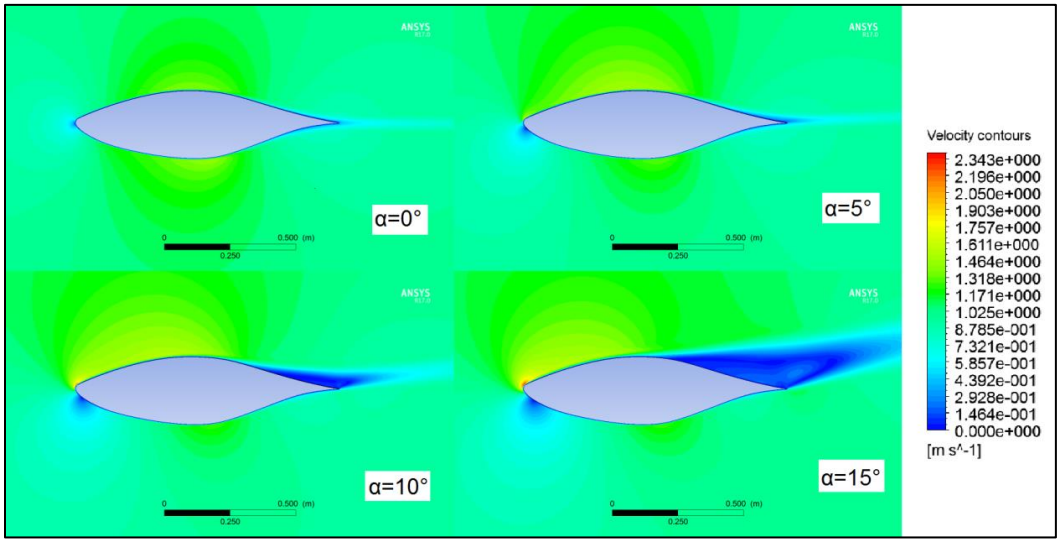

Fig. 16. Velocity distributions of tuna fish hydrofoil hydrofoil at Re=1 million (Muratoglu and Muratoglu 2017)

It would be more accurate and feasible to compare tope shark hydrofoil generated and analyzed in this study with existing man-designed hydrofoils which are generated or specially preferred to be used in water environment. Although majority of airfoils are generated for air environment, there are several profiles which are suitable to be employed in the water environment such as

NACA-63, NREL-S or RISØ-A family of airfoils. Distribution of pressure coefficients over around the NACA 36-818, NREL S833, RISØ-A-18 and TSH profiles at the same Re number and approximate angles of attack were provided in Figure 17 for better comparison. According to the figure, TSH which is originated through this study exhibits superior performance in terms of having lower pressure coefficient margins which is a very important criteria for cavitation inception.

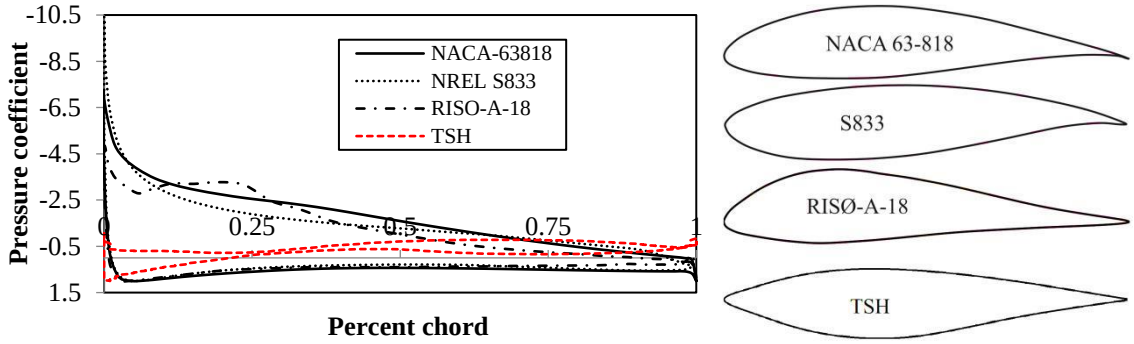

Fig. 17. Comparison of pressure coefficients for NACA 36-818, NREL S833, RISØ-A-18 (Re=1 million, α=12°) and TSH (Re=1 million, α=10°)

Finally comparison of lift and drag characteristics of abovementioned man-designed airfoils with the TSH is given in Figure 18. These airfoils are among the widely used sections of wind or hydrokinetic turbines. Tope shark hydrofoil (TSH) has relatively low drag and lift performance from the power generation or other aeronautical or hydrodynamic points of view. As it described in Section 3.4, delivering high lift force may block important living activities of the tope shark. It is obvious that, TSH body geometry is not naturally optimized for power production or maximization of the lift. Therefore, comparing TSH with the existing airfoils of higher lift performance would be rather inconvenient. However, special considerations could be intensified on the power coefficient distribution of its body shape. Superior performance of TSH against cavitation at a wide range of angle of attack could be a point of inspiration for marine technologies.

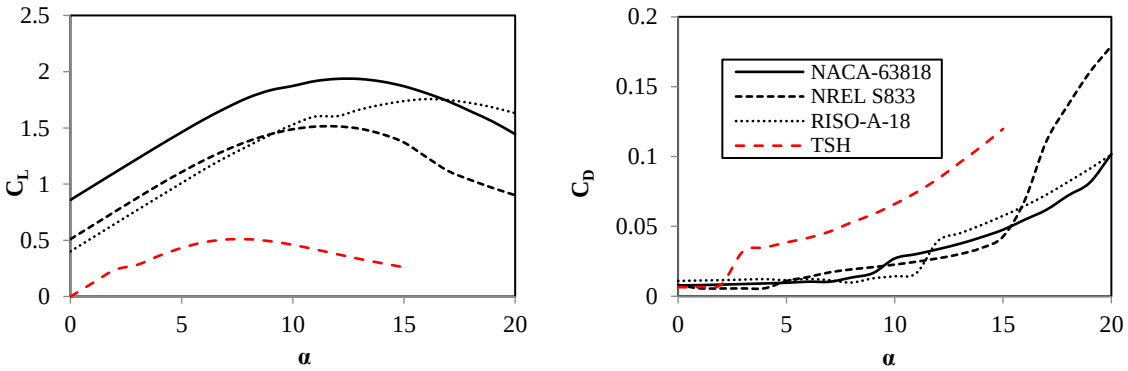

Fig. 18. Lift and drag characteristics of NACA 63-818, NREL S833, RISØ-A-18 and TSH profiles at Re=1x10^6

4. CONCLUSION

The hydrodynamics of tope shark hydrofoil (TSH) has been underlined in the present study. The flow fields of pressure and velocity have been illustrated numerically for different dynamic and geometrical conditions. The TSH has been analyzed based on the airfoil/hydrofoil theory of man-designed sections. It should be noted that, TSH exhibits the behavior of classical airfoils and fits the methodology. Secondly, the geometry of the tope shark body (excluding the caudal, pectoral, anal dorsal and pelvic fins) contributes to the swimming performance with relatively lower pressure coefficient and considerable amount of lift to withstand gravity together with other buoyancy forces. The stall angle of TSH has been determined to be 7-8 degrees with a smooth C_L-α curve around the stall region. The CFD simulation results have been validated using JavaFoil (Hepperle 2014) software. Future studies will make possible to adapt natural body shapes of the swimming animals to energy and aviation technologies such as turbine blades (Muratoglu et al. 2017) or aircraft wing sections.

REFERENCES

Anderson Jr, J. (2011). Fundamentals of Aerodynamics. Mc. Graw-Hill, New York.

ANSYS. (2011). Introduction to ANSYS CFX, Lecture notes on Turbulence.

Bandyopadhyay, P. R. (2002). “Maneuvering hydrodynamics of fish and small underwater vehicles.” Integrative and comparative biology, 42(1), 102–117.

Bone, Q., and Moore, R. H. (2013). Biology of Fishes. Journal of Chemical Information and Modeling.

Bozkurttas, M., Tangorra, J., Lauder, G., and Mittal, R. (2008). "Understanding the Hydrodynamics of Swimming: From Fish Fins to Flexible Propulsors for Autonomous Underwater Vehicles." Advances in Science and Technology, 58, 193–202.

Camhi, M. D., Lauck, E., Pikitch, E. K., and Babcock, E. A. (2009). "A Global Overview of Commercial Fisheries for Open Ocean Sharks." Sharks of the Open Ocean: Biology, Fisheries and Conservation, 166–192.

Çengel, Y. A., and Cimbala, J. M. (2006). "Fluid mechanics: fundamentals and applications." Fluid Mechanics: With Problems and Solutions, and an Aerodynamic Laboratory, 956.

Dahl, K. S., and Fuglsang, P. (1998). Design of the wind turbine airfoil family Risø-A-XX. Design of the Wind Turbine Airfoil Family RISØ-A-XX, Roskilde, Denmark.

Francis, M. P., and Mulligan, K. P. (1998). "Age and growth of New Zealand school shark, Galeorhinus galeus." New Zealand Journal of Marine and Freshwater Research, 32(3), 427–440.

Grasso, F. (2012). "Design and Optimization of Tidal Turbine Airfoil." Journal of Aircraft, 49(2), 636–643.

Hemelrijk, C. K., Reid, D. A. P., Hildenbrandt, H., and Padding, J. T. (2015). "The increased efficiency of fish swimming in a school." Fish and Fisheries, 16(3), 511–521.

Hepperle, M. (2014). "JavaFoil."

Hurst, R. J., Baglet, N. W., McGregor, G. A., and Francis, M. P. (1999). "Movements of the New Zealand school shark, Galeorhinus galeus, from tag returns." New Zealand Journal of Marine and Freshwater Research, 33(1), 29–48.

Lauder, G. V, and Drucker, E. G. (2004). "Morphology and experimental hydrodynamics of fish fin control surfaces." IEEE Journal of Oceanic Engineering, 29(3), 556–571.

Lauder, G. V, and Madden, P. G. A. (2006). "Learning from fish: Kinematics and experimental hydrodynamics for roboticists." International Journal of Automation and Computing, 3(4), 325–335.

Mauclère, X. (2009). "Automatic 2D Airfoil Generation, Evaluation and Optimisation using MATLAB and XFOIL." Mycotoxin research.

Muratoglu, A. (2014). "Design and simulation of a riverine hydrokinetic turbine." University of Gaziantep.

Muratoglu, A., and Muratoglu, A. (2017). "Understanding hydrodynamics of Tuna Fish hydrofoil using CFD simulations." 7th Ankara International Aerospace Conference (AIAC'2017), Ankara.

Muratoglu, A., Ph, D., Yuce, M. I., and Ph, D. (2017). "Design of a River Hydrokinetic Turbine Using Optimization and CFD Simulations."

Muratoglu, A., Yuce, M. I., and Esit, M. (2016). "Foil generation inspiring from nature." International Conference on Natural Science and Engineering (ICNASE'16), Kilis.

Rubenstein, D. A., Yin, W., and Frame, M. D. (2012). "Fundamentals of Fluid Mechanics." Biofluid Mechanics, 11–48.

Shrivastava, M., Malushte, M., Agrawal, A., and Sharma, A. (2017). "CFD study on hydrodynamics of three fish-like undulating hydrofoils in side-by-side arrangement." Lecture Notes in Mechanical Engineering, Part F8, 1443–1451.

Triantafyllou, M. S. (2012). "Survival hydrodynamics." Journal of Fluid Mechanics, 698, 1–4.

Tytell, E. D. (2011). Experimental hydrodynamics. Encyclopedia of Fish Physiology: From Genome to Environment.

Versteeg, K. H., and Malalasekera, W. (2007). Computational Fluid Dynamics. McGraw-Hill, Inc.

Vincent, J. F. V, Bogatyreva, O. A., Bogatyrev, N. R., Bowyer, A., and Pahl, A.-K. (2006). "Biomimetics: its practice and theory." Journal of The Royal Society Interface, 3(9), 471–482.

Wang, Q., Chen, J., Pang, X., Li, S., and Guo, X. (2013). "A new direct design method for the medium thickness wind turbine airfoil." Journal of Fluids and Structures, 43, 287–301.

Webb, P. W. (1978). "Hydrodynamics: Nonscombroid fish." Fish Physiology, 7(C), 189–237.

Weihs, D. (1980). "Hydrodynamics of suction feeding of fish in motion." Journal of Fish Biology, 16(4), 425–433.

White, F. (2010). “Fluid Mechanics.” McGraw-Hill,New York, 862.

Xue, G., Liu, Y., Zhang, M., and Ding, H. (2016). “Numerical Analysis of Hydrodynamics for Bionic Oscillating Hydrofoil Based on Panel Method.” Applied Bionics and Biomechanics, 2016.

Yuce, M. I., and Muratoglu, A. (2015). “Hydrokinetic energy conversion systems: A technology status review.” Renewable and Sustainable Energy Reviews, 43, 72–82.